Research Square

Preprints are preliminary reports that have not undergone peer review.
They should not be considered conclusive, used to inform clinical practice,
or referenced by the media as validated information.

Characterization and archived CO_2 hydrogenation data for bimetallic catalysts on octahedral ceria

Muhammad Usman Aslam
China University of Petroleum, Beijing
Qi Liu
liuqi@cup.edu.cn

China University of Petroleum, Beijing
Shengkun Wu
China University of Petroleum, Beijing
Chunkai Wang
China University of Petroleum, Beijing
Farzand Ali
China University of Petroleum, Beijing
Muhammad Azam Khan
China University of Petroleum, Beijing

Research Article

Keywords: CO_2 hydrogenation, octahedral ceria, reverse water-gas shift, methanation, bimetallic catalysts, data reconciliation

Posted Date: October 21st, 2026

DOI: https://doi.org/10.21203/rs.3.rs-11290027/v1

License: This work is licensed under a Creative Commons Attribution 4.0 International License.
Read Full License

Additional Declarations: No competing interests reported.

Abstract

CO_2 hydrogenation can yield carbon monoxide through reverse water-gas shift or methane through methanation, making reliable sample provenance and carbon accounting essential for catalyst comparison. This work examines octahedral CeO_2-supported CuNi, FeCu, and AuRu formulations using available characterization and archived catalytic records. Scanning electron microscopy (SEM) shows faceted ceria particles, while energy-dispersive X-ray spectroscopy (EDS) supports local Cu/Ni and Fe/Cu co-presence. AuRu elemental quantification differs between the archived report and manuscript figure. The archived summary suggests temperature-dependent differences in normalized CO/CH_4 distributions, with CuNi- and FeCu-labelled series relatively CO-rich at elevated temperature and an AuRu-labelled series showing a methane-rich interval. Sample-to-run links, conversion scaling, and catalyst-mass/flow bases remain unresolved. Recalculation repairs a recoverable carbon-product denominator error and includes recorded C_2/C_3 products, but does not establish sample identity or independent inlet–outlet carbon closure.

1. Introduction

The catalytic hydrogenation of CO_2 has attracted sustained attention because it can couple greenhouse-gas utilization with the production of fuels and chemical intermediates (Olah et al. 2009). Under hydrogen-rich conditions, two C1 pathways are especially important, the Sabatier methanation reaction, $CO_2 + 4H_2 \rightleftharpoons CH_4 + 2H_2O$, and the reverse water-gas shift (RWGS) reaction, $CO_2 + H_2 \rightleftharpoons CO + H_2O$ (Ebrahimi et al. 2022). The first pathway produces methane directly, whereas the second generates CO, a key syngas component for downstream synthesis. A central challenge is therefore to tune the catalyst so that CO_2 activation, hydrogen dissociation, surface oxygen removal, and product desorption are balanced toward the desired product.

CeO_2 is a useful support because its Ce^{4+}/Ce^{3+} redox cycle is associated with oxygen mobility and vacancy formation (Trovarelli and Llorca 2017). Ceria facets can influence supported-metal speciation and CO_2 hydrogenation behavior (Jiang et al. 2020; An et al. 2024). Cu- and Fe-containing ceria formulations have been investigated for CO production (Chen et al. 2021; Zhou et al. 2020), whereas Ni- and Ru-containing systems have been studied for methanation (Liao et al. 2024; Wang et al. 2016). These precedents motivate a comparison of the present formulations without establishing their working structures or relative performance in advance.

The two target products place different demands on a catalyst. CO production requires carbon dioxide activation followed by release of a partially reduced carbon product. Methane formation requires additional hydrogenation and removal of oxygen as water. A formulation that activates CO_2 readily can therefore remain selective to CO if the resulting carbon species leaves the surface before further hydrogenation. Conversely, retention of reactive carbon intermediates near sites that supply hydrogen can favor methane. This competition makes product distribution an essential part of catalyst screening: increased CO_2 consumption alone does not identify the preferred pathway.

Ceria morphology provides a useful starting point for organizing this competition, but shape is not a complete description of the working interface. Jiang et al. related support facets to vacancy behavior and Pd speciation in methanol synthesis (Jiang et al. 2020). An et al. showed that ceria shape also changes the selectivity of singly dispersed Ru catalysts, linking CO affinity and hydrogen activation to the supported Ru state (An et al. 2024). These studies concern different active phases and products; their relevance here is that the same oxide composition can support chemically different reaction environments. An octahedral particle habit consequently motivates a comparison within a defined morphology, without establishing that every formulation contains the same active surface.

The selected metal pairs allow this question to be examined across base-metal and noble-metal formulations. The Cu–Fe/CeO_2 study of Chen et al. provides a directly related precedent for CO production (Chen et al. 2021), whereas the Ni/CeO_2 studies of Du et al. and Zhu et al. concern methane formation on vacancy-rich or vacancy-engineered materials (Du et al. 2021; Zhu et al. 2021). These precedents motivate testing the present formulations but do not establish synergy in advance. A bimetallic designation identifies the elements introduced during preparation; demonstrating cooperation between them would additionally require comparisons with the corresponding single-metal catalysts.

The comparison distinguishes CO_2 conversion, normalized CO/CH_4 fractions, and two-product rate estimates. These quantities represent different calculations and cannot independently confirm one another. The octahedral description applies to the supplied characterization images; it does not establish the morphology of every specimen represented in the catalytic worksheets. Differences in preparation history also prevent assigning performance differences solely to elemental composition. The present analysis therefore assesses the calculation chain and the evidence available for formulation-associated product trends.

1.1 Research objective and scope

The objective is to assess the available evidence for temperature-dependent CO_2 conversion and CO/CH_4 product distributions in CuNi, FeCu, and AuRu formulations associated with octahedral CeO_2, while distinguishing verified specimen characterization from catalytic quantities whose sample provenance remains incomplete.

The analysis asks whether the available records support reproducible formulation-associated differences in CO-rich and methane-rich outlets under comparable conditions. Because preparation histories and sample-to-run links are incomplete, the present work emphasizes evidence-supported trends and data reconciliation rather than an intrinsic activity ranking.

2. Experimental

This section reports the recorded synthesis and characterization procedures, reaction protocol, and calculation definitions used in the analysis. Where batch-specific information is unavailable, the limitation is stated explicitly rather than reconstructed from unrelated specimens.

2.1 Materials

The preparation descriptions list cerium(III) nitrate hexahydrate, disodium hydrogen phosphate, deionized water, and ethanol for the ceria support; copper and nickel nitrate precursors for CuNi; and copper and iron nitrate precursors for FeCu. $CeCl_3 \cdot 7H_2O$, $RuCl_3 \cdot nH_2O$, $HAuCl_4 \cdot 4H_2O$, and NaOH are listed for AuRu. The supplied method also lists H_2, CO_2, N_2, and He for reaction testing and gas analysis. Complete batch-specific supplier, purity, and hydrate information is not established by the surviving preparation descriptions.

2.2 Synthesis of octahedral CeO_2

The recorded support procedure dissolves $Ce(NO_3)_3 \cdot 6H_2O$ (1.716 g) and a phosphate reagent (0.015 g) in 160 mL of deionized water. The reagent is named disodium hydrogen phosphate in the materials list, but the recorded formula is inconsistent and the hydrate is unspecified. After approximately 30 min of stirring, the mixture is transferred to a PTFE-lined autoclave and heated at 170°C for 10 h. The product is washed with deionized water and ethanol, centrifuged, dried at 80°C overnight, and calcined in air at 400°C for 4 h.

2.3 Preparation of octahedral CeO_2-supported bimetallic catalysts

2.3.1 CuNi/CeO_2-O

The CuNi preparation description uses wet impregnation of octahedral CeO_2 (0.27 g) with an aqueous copper/nickel nitrate solution. The suspension is sonicated for 60 min, stirred at 80°C until evaporation, held at 100°C overnight, ground, and calcined at 450°C for 4 h. The surviving octahedral preparation record does not specify precursor quantities, hydration states, solution volume or concentrations, nominal metal ratio or loading, or calcination atmosphere. These missing batch-specific quantities were not inferred from preparation records for other specimens.

2.3.2 FeCu/CeO_2-O

The FeCu preparation description uses wet impregnation of octahedral CeO_2 (0.27 g) with an aqueous copper/iron nitrate solution. The suspension is sonicated for 60 min, stirred at 70°C until evaporation, held at 60°C overnight, ground, and calcined at 450°C for 4 h under Ar. The surviving description does not establish the nitrate hydration states, quantities, impregnation volume or concentrations, target Fe:Cu ratio, or nominal loading for the octahedral sample.

2.3.3 AuRu/CeO_2-O

The recorded AuRu preparation uses co-precipitation followed by hydrothermal treatment and calcination. $CeCl_3 \cdot 7H_2O$ (3.8 mmol), $RuCl_3 \cdot nH_2O$ (0.2 mmol), and $HAuCl_4 \cdot 4H_2O$ (0.5 g) were dissolved in 10 mL of deionized water. The solution was added gradually to 70 mL of vigorously stirred 7 M NaOH, producing a black precipitate. After 30 min of aging, the mixture was sealed in a PTFE-lined autoclave

and heated at 140°C for 48 h. The product was centrifuged, washed with water and isopropanol, vacuum-dried at room temperature, ground, and calcined in air at 400°C for 4 h. These quantities describe precursor input and do not establish retained bulk metal loading.

2.4 Catalyst characterization

The supplied characterization method lists scanning electron microscopy with energy-dispersive X-ray spectroscopy (SEM–EDS) using an FEI 200F instrument at 5 kV, and X-ray diffraction (XRD) using a Bruker D8 with Cu Kα radiation and a Ni filter. The draft specifies a 5–90° 2θ scan at 4° min⁻¹, with 40 kV and 30 mA operation; these acquisition settings are not independently established by the recovered numerical scan files. Nitrogen physisorption was recorded at 77 K after vacuum degassing at 150°C for 3 h. Surface area and pore analysis use the Brunauer–Emmett–Teller and Barrett–Joyner–Halenda methods, respectively (Brunauer et al. 1938; Barrett et al. 1951). Interpretation follows the distinction between surface area, pore filling, and model-dependent pore-size estimates described by Thommes et al. (2015).

2.5 Catalytic evaluation, gas analysis, and calculation framework

The recorded reaction protocol specifies an 8 mm internal-diameter fixed-bed reactor, 0.30 g of catalyst diluted with 0.20 g of silica sand, H_2 reduction at 350°C for 2 h at 50 mL min⁻¹, and reaction at 3.0 MPa. The nominal $CO_2/H_2/N_2$ flows are 10/30/10 mL min⁻¹, with 35 min stabilization at each temperature. On this stated mass basis, 50 mL min⁻¹ corresponds to a mass-specific volumetric feed rate of 10,000 mL gcat⁻¹ h⁻¹; it is not a volume-based gas hourly space velocity. Gas analysis was recorded using thermal conductivity and flame ionization detectors with molecular sieve 5A and Porapak Q columns. Because archived calculation files contain inconsistent mass and flow labels, calculations based on the nominal protocol are treated as conditional unless linked to a specific run.

Equations (1) and (2) define CO_2 conversion XCO_2 and the normalized two-product fraction s_i as fractions, rather than percentages. In Eq. (2), i denotes CO or CH_4. Eq. (3) assigns all converted inlet CO_2 to that restricted product pool to obtain a two-product rate estimate. This estimate requires the stated mass and inlet-flow convention and does not independently measure product formation.

$$X_{\mathrm{CO_2}} = \frac{F_{\mathrm{CO_2,in}} - F_{\mathrm{CO_2,out}}}{F_{\mathrm{CO_2,in}}}$$

1

$$s_i = \frac{F_{i,\mathrm{out}}}{F_{\mathrm{CO,out}} + F_{\mathrm{CH_4,out}}} \qquad (2)$$

$$r_{i,2p} = \frac{F_{CO,in}\, X_{CO}\, s_i}{m_{cat}} \qquad (3)$$

Here, F denotes molar flow, mcat is catalyst mass, and XCO_2 and s_i are fractions; percentages equal 100 times those fractions. The subscript 2p denotes the two-product assumption. The summary uses 10 mL min^{-1} of inlet CO_2, 0.30 g of catalyst, and 24.465 L mol^{-1} at 25°C and 1 atm. This convention gives approximately 81,749 µmol g^{-1} h^{-1} of inlet CO_2. The resulting rates are arithmetic estimates and remain conditional on the unresolved mass and flow records. Recorded C_2/C_3 products invalidate complete carbon accounting based only on CO and CH_4.

2.6 Experimental design and reporting boundaries

For mutually comparable calibrated concentrations, the composition-based correction is $X^* = P/(cCO_2 + P)$, where $P = cCO + cCH_4 + 2(cC_2H_6 + cC_2H_4) + 3(cC_3H_8 + cC_3H_6)$. Several worksheet blocks omit P through a shifted denominator reference. The corrected carbon-product fraction is $S_i,C = n_i c_i/P$, where n_i is the product carbon number. Both quantities are fractions; multiply by 100 to report percentages. All-zero denominators remain undefined. These conditional expressions include the recorded products but assume a common calibration basis and complete carbon accounting. They do not measure an independent inlet–outlet carbon balance.

The recovered records do not establish independent preparation or reaction replicates, so uncertainty estimates and significance tests are unavailable. Repeated temperature points and photo/thermal files are not treated as independent replicates. All-zero source blocks are undefined analytical records rather than confirmed non-detection. The temperature sequence alone does not establish stability, deactivation, or intrinsic kinetics.

2.7 Data reconciliation and comparison criteria

The analysis is restricted to specimens described as octahedral CeO_2-supported catalysts. A complete one-to-one link among preparation batch, characterized specimen, catalytic run, and calculation file could not be reconstructed for every record. Consequently, conflicting sample labels, conversion scaling, and mass/flow inputs are treated as provenance limitations rather than resolved by assumption. Figure 4 and Table 1 are retained as archived catalytic summaries to show the reported trends and the calculation chain; they are not used as a validated activity ranking. Records assigned to other support morphologies are excluded from the experimental comparison. The listed 50.94% CuNi conversion also appears in the published cubic-ceria screening study (Aslam et al. 2026). It is not treated here as an independently verified octahedral-catalyst result.

3. Results and discussion

3.1 Octahedral morphology and elemental distribution

The supplied SEM and EDS images show faceted ceria particles and local Ce/O co-distribution (Fig. 1). The morphology is consistent with the octahedral description of the support image. It does not by itself establish a shared batch or morphology for the specimens associated with every catalytic worksheet.

3.2 Crystal structure and textural properties

The supplied diffraction illustration is labelled for AuRu/CeO_2-O, FeCu/CeO_2-O, and CuNi/CeO_2-O and includes reference markers for ceria (Fig. 2). However, the original sample-specific numerical scans and their angular calibration were not recovered in a form that resolves the figure provenance. Detailed plane assignments, metal-phase claims, and quantitative comparisons of peak shifts or widths are therefore not made here.

The supplied nitrogen-physisorption analysis for the specimen labelled octahedral CeO_2 reports a BET surface area of 3.81 $m^2\ g^{-1}$ and a pore volume of 0.023 mL g^{-1}. The volume-to-area ratio 4V/A gives approximately 24.1 nm; this is a geometric estimate, not a BJH mean pore diameter. The low uptake and rise near saturation may include external-surface and interparticle-void contributions (Fig. 3). Without adsorption measurements for each loaded catalyst, the support isotherm cannot establish equal accessible area or intrinsic area-normalized rates. Metal dispersion, oxidation state, bulk loading, and interfacial density remain unresolved.

3.3 Archived catalytic trends and data reconciliation

Table 1 and Fig. 4 summarize the archived 350°C catalytic values. The records list CO_2 conversions of 21.50%, 50.94%, and 44.24% for AuRu-, CuNi-, and FeCu-labelled series, with normalized CO fractions of 34.10%, 73.42%, and 67.97%, respectively. Under the two-product convention of Eq. (3), the corresponding rounded CO rate estimates are 5,993, 30,575, and 24,583 μmol $g^{-1}\ h^{-1}$. These quantities reproduce the archived calculation chain and describe differences between labelled series.

Table 1
Archived catalytic summary at 350°C. Values reproduce the recorded calculation chain; sample-to-run identity and conversion basis require validation before quantitative catalyst ranking.

Catalyst label	Listed CO_2 conversion (%)	CO rate estimate (μmol $g^{-1}\ h^{-1}$)	CH_4 rate estimate (μmol $g^{-1}\ h^{-1}$)	Normalized CO fraction (%)	Normalized CH_4 fraction (%)
AuRu/CeO_2-O	21.50	5,993	11,583	34.10	65.90
CuNi/CeO_2-O	50.94	30,575	11,068	73.42	26.58
FeCu/CeO_2-O	44.24	24,583	11,583	67.97	32.03

The CO and CH_4 rate estimates sum to the assigned converted inlet CO_2 by construction and therefore do not provide an independent carbon balance. Quantitative comparison requires sample-linked calibrated concentrations, actual inlet and outlet molar flows, catalyst masses, and gas reference states.

3.3.1 Temperature-dependent conversion trends

In the summary, the AuRu-labelled series rises to 20.50% conversion at 250°C and approaches 21.50% at 350°C. The CuNi-labelled series rises from 4.00% at 250°C to 50.94% at 350°C, while the FeCu-labelled series is non-monotonic below 300°C before reaching 44.24% at 350°C. These profiles document the reported temperature response, but mechanistic interpretation is not attempted because the underlying series are not fully reconciled with the characterized specimens.

3.3.2 Evolution of normalized CO and methane fractions

The archived summary shows a methane-rich intermediate/high-temperature interval for the AuRu-labelled series, a transition from methane-rich low-conversion entries to CO-rich high-temperature entries for the CuNi-labelled series, and a predominantly CO-rich FeCu-labelled series. These normalized CO/CH_4 fractions are not equivalent to full carbon selectivities when additional C_2/C_3 products are present. All-zero analytical blocks are treated as undefined rather than as evidence of complete selectivity.

3.3.3 Relationship between normalized fractions and rate estimates

The two-product estimates combine the listed conversion and normalized product fraction through Eq. (3). They therefore inherit both uncertainties and cannot serve as independent confirmation of the summary trends. Conditional corrections to the archived concentration-based denominators produce different conversions, but importing those corrections into the manuscript would require a defensible link between the specific records and the characterized catalysts.

3.4 Context from related ceria-supported catalysts

Published ceria-supported catalysts provide context for the possible competition between CO production and methanation. The unresolved provenance of the present summary prevents using that comparison to establish composition-dependent performance or bimetallic synergy.

Ni/CeO_2 studies associate methanation with vacancy chemistry and metal–support interfaces (Liao et al. 2024; Du et al. 2021; Zhu et al. 2021; Bhat et al. 2024). Related work addresses the identity of active sites directly (Tada et al. 2021). These studies motivate surface-sensitive characterization of CuNi formulations, but SEM–EDS cannot determine whether Cu dilutes contiguous Ni sites or changes their reaction pathway.

$Cu–Fe/CeO_2$ and Cu/CeO_2 studies provide relevant examples of CO-forming catalysts (Chen et al. 2021; Zhou et al. 2020). Co-detection of Fe and Cu in the present images establishes local elemental presence. It does not identify the exposed working phase or establish that the provisional catalytic summary originated from that specimen.

An et al. (2024) studied shape-dependent behavior of singly dispersed Ru on ceria, while Wang et al. (2016, 2023) examined Ru/CeO_2 methanation and loading effects. These results illustrate why Ru

presence alone cannot specify a unique product pathway. A matched Ru-only control and direct structural characterization would be required to isolate any effect of Au in the present formulation.

3.5 Elemental mapping of octahedral bimetallic catalysts

The CuNi-labelled EDS report lists 55.58 wt.% Ce, 17.97 wt.% O, 14.24 wt.% Cu, and 12.20 wt.% Ni, matching the values in the supplied figure. The maps and spectrum support local Cu/Ni co-presence in the analyzed ceria-containing region (Fig. 5). These region-specific fractions do not establish alloy formation, bulk loading, or the identity of a catalytic run.

The supplied AuRu figure lists 31.59 wt.% Ce, 15.12 wt.% O, 32.29 wt.% Au, and 21.00 wt.% Ru. In contrast, the archived AuRu-labelled EDS report lists 38.59 wt.% Ce, 22.12 wt.% O, 39.29 wt.% Au, and 0.00 wt.% Ru. Whether these records represent different regions, specimens, or processing cannot be established. The figure is retained for traceability (Fig. 6), but its Au/Ru fractions and local Au–Ru co-presence are not treated as verified. A zero reported Ru fraction in one region does not establish absence throughout the catalyst.

The archived FeCu-labelled EDS report lists 54.90 wt.% Ce, 26.28 wt.% O, 12.55 wt.% Fe, and 6.27 wt.% Cu, matching the supplied figure. It supports local Fe/Cu co-presence in the analyzed ceria-containing region (Fig. 7). The summed local metal fractions are 26.44 wt.% for CuNi and 18.82 wt.% for FeCu. The AuRu records disagree, so its summed fraction is not used in a composition comparison. Local EDS fractions are neither bulk catalyst loadings nor evidence of matched metal contents.

For the CuNi- and FeCu-labelled specimens, the maps support local elemental co-presence rather than atomic-scale metal contact. SEM–EDS overlap cannot distinguish an alloy, adjacent particles, mixed oxides, or separate species within the same interaction volume.

3.6 Reaction pathway context

CO and methane formation can be discussed in terms of reverse water-gas shift and methanation chemistry (Ebrahimi et al. 2022; Wang et al. 2016). Observing both outlet products does not distinguish sequential CO hydrogenation from parallel pathways. Surface intermediates and active ensembles were not measured in the present study.

Ceria surface chemistry and metal-mediated hydrogen activation are plausible contributors to product distribution. They remain literature-informed hypotheses for these specimens, rather than mechanisms established by the provisional catalytic summary. Atomic-scale structure and operando evidence would be needed to connect a reconciled product trend to an active site.

3.7 Validation requirements and study limitations

The principal limitation is incomplete traceability between characterized specimens and catalytic records. The archived files contain incompatible morphology labels, approximately threefold conversion scaling in some comparisons, and inconsistent catalyst-mass and flow bases. These discrepancies can

change both the magnitude and direction of an apparent catalyst ranking; correcting a carbon-product denominator alone cannot resolve sample provenance.

The octahedral CuNi and FeCu preparation descriptions omit precursor quantities and chemical forms needed to reproduce metal loading. Complete sample-specific recipes and a documented link to the characterized specimens are therefore required. The intended shared octahedral morphology and reaction protocol do not establish that all catalytic files represent those specimens under comparable conditions.

For a CO_2-only carbon feed, carbon closure is $B_C = (F_{CO_2,out} + \Sigma\, n_i F_{i,out})/F_{CO_2,in}$, with every quantified carbon product included. Percentage closure is $100B_C$. Residual CO_2 and product concentrations alone cannot establish this flow balance. Independent preparation and reaction replicates are also needed to quantify uncertainty. No carbon-closure value, error bar, significance test, or replication count is assigned to the present summaries.

The study does not establish long-term durability. Stabilization for 35 min at each temperature does not exclude slow activation, deactivation, sintering, or oxidation-state drift. Extended time-on-stream tests, heating–cooling cycles, and post-reaction characterization would determine whether the reported product distributions persist. Independent inlet and outlet carbon inventories and matched bulk metal loadings are priorities for validating the comparison.

4. Conclusions

Faceted ceria morphology consistent with the intended octahedral support was observed, and SEM–EDS supported local Cu/Ni and Fe/Cu elemental co-presence. The archived catalytic summary suggested distinct normalized CO/CH_4 patterns: CuNi- and FeCu-labelled series were relatively CO-rich at elevated temperature, whereas the AuRu-labelled series showed a comparatively methane-rich interval. These preliminary patterns motivate investigation of formulation effects on reverse water-gas shift and methanation. Their assignment to the characterized octahedral catalysts remains unresolved, preventing a validated performance comparison. Conflicting AuRu elemental quantification and incomplete carbon closure further limit interpretation.

Statements and Declarations

Acknowledgments

The authors acknowledge the analytical and laboratory facilities of the School of Chemical Engineering and Environmental Sciences, China University of Petroleum (Beijing).

Author contributions. Muhammad Usman Aslam: Investigation, Data curation, Formal analysis, Visualization, Writing – original draft. Shengkun Wu: Data curation, Visualization. Chunkai Wang: Data

curation, Visualization. Farazand Ali: Visualization. Muhammad Azam Khan: Visualization. Qi Liu: Supervision, Resources, Writing – review and editing.

Funding. This work was supported by the National Natural Science Foundation of China (grant number 52574060).

Competing interests. The supplied declaration states that the authors have no competing financial interests. A declaration covering non-financial interests is not established by the available materials.

Use of generative artificial intelligence tools

Generative AI tools were used for language editing, document review, source-record comparison, and assistance with calculation checks.

Data availability

The available characterization reports, archived catalytic summaries, and conditional calculation records are retained in the study.

References

1. An Z, Ma N, Xu Y, Yang H, Zhao H, Wu L, Tan L, Zou C, Meng F, Zhang B, Wang X, Tang Y (2024) Shape dependency of CO_2 hydrogenation on ceria supported singly dispersed Ru catalysts. J Catal 429:115245. https://doi.org/10.1016/j.jcat.2023.115245
2. Aslam MU, Aziz S, Ahmad A, Liu Q (2026) Preliminary performance screening of cubic CeO_2 supported bimetallic catalysts for CO_2 hydrogenation. Chem Pap. https://doi.org/10.1007/s11696-026-05580-0
3. Barrett EP, Joyner LG, Halenda PP (1951) The Determination of Pore Volume and Area Distributions in Porous Substances. I. Computations from Nitrogen Isotherms. J Am Chem Soc 73:373–380. https://doi.org/10.1021/ja01145a126
4. Bhat S, Sepúlveda-Pagán M, Borrero-Negrón J, Meléndez-Gil JE, Nikolla E, Pagán-Torres YJ (2024) Effects of catalyst morphology on oxygen defects at Ni–CeO_2 interfaces for CO_2 methanation. Catal Sci Technol 14:3364–3373. https://doi.org/10.1039/d4cy00173g
5. Brunauer S, Emmett PH, Teller E (1938) Adsorption of Gases in Multimolecular Layers. J Am Chem Soc 60:309–319. https://doi.org/10.1021/ja01269a023
6. Chen L, Wu D, Wang C, Ji M, Wu Z (2021) Study on Cu-Fe/CeO_2 bimetallic catalyst for reverse water gas shift reaction. J Environ Chem Eng 9:105183. https://doi.org/10.1016/j.jece.2021.105183
7. Du Y, Qin C, Xu Y, Xu D, Bai J, Ma G, Ding M (2021) Ni nanoparticles dispersed on oxygen vacancies-rich CeO_2 nanoplates for enhanced low-temperature CO_2 methanation performance. Chem Eng J 418:129402. https://doi.org/10.1016/j.cej.2021.129402

8. Ebrahimi P, Kumar A, Khraisheh M (2022) A Review of CeO_2 Supported Catalysts for CO_2 Reduction to CO through the Reverse Water Gas Shift Reaction. Catalysts 12:1101. https://doi.org/10.3390/catal12101101
9. Jiang F, Wang S, Liu B, Liu J, Wang L, Xiao Y, Xu Y, Liu X (2020) Insights into the Influence of CeO_2 Crystal Facet on CO_2 Hydrogenation to Methanol over Pd/CeO_2 Catalysts. ACS Catal 10:11493–11509. https://doi.org/10.1021/acscatal.0c03324
10. Liao L, Wang K, Liao G, Nawaz MA, Liu K (2024) Oxygen vacancy-dependent low-temperature performance of Ni/CeO_2 in CO_2 methanation. Catal Sci Technol 14:6537–6549. https://doi.org/10.1039/D4CY00679H
11. Olah GA, Goeppert A, Prakash GKS (2009) Chemical Recycling of Carbon Dioxide to Methanol and Dimethyl Ether: From Greenhouse Gas to Renewable, Environmentally Carbon Neutral Fuels and Synthetic Hydrocarbons. J Org Chem 74:487–498. https://doi.org/10.1021/jo801260f
12. Tada S, Nagase H, Fujiwara N, Kikuchi R (2021) What Are the Best Active Sites for CO_2 Methanation over Ni/CeO_2? Energy Fuels 35:5241–5251. https://doi.org/10.1021/acs.energyfuels.0c04238
13. Thommes M, Kaneko K, Neimark AV, Olivier JP, Rodriguez-Reinoso F, Rouquerol J, Sing KSW (2015) Physisorption of gases, with special reference to the evaluation of surface area and pore size distribution (IUPAC Technical Report). Pure Appl Chem 87:1051–1069. https://doi.org/10.1515/pac-2014-1117
14. Trovarelli A, Llorca J (2017) Ceria Catalysts at Nanoscale: How Do Crystal Shapes Shape Catalysis? ACS Catal 7:4716–4735. https://doi.org/10.1021/acscatal.7b01246
15. Wang F, He S, Chen H, Wang B, Zheng L, Wei M, Evans DG, Duan X (2016) Active Site Dependent Reaction Mechanism over Ru/CeO_2 Catalyst toward CO_2 Methanation. J Am Chem Soc 138:6298–6305. https://doi.org/10.1021/jacs.6b02762
16. Wang C, Sun H, Liu X, Jin X, Feng Y, Shi H, Wang D, Zhang Y, Wang Y, Yan Z (2023) Low-temperature CO_2 methanation over Ru/CeO_2: Investigation into Ru loadings. Fuel 345:128238. https://doi.org/10.1016/j.fuel.2023.128238
17. Zhou G, Xie F, Deng L, Zhang G, Xie H (2020) Supported mesoporous Cu/CeO_2-δ catalyst for CO_2 reverse water–gas shift reaction to syngas. Int J Hydrogen Energy 45:11380–11393. https://doi.org/10.1016/j.ijhydene.2020.02.058
18. Zhu M, Tian P, Cao X, Chen J, Pu T, Shi B, Xu J, Moon J, Wu Z, Han YF (2021) Vacancy engineering of the nickel-based catalysts for enhanced CO_2 methanation. Appl Catal B Environ 282:119561. https://doi.org/10.1016/j.apcatb.2020.119561

Figures

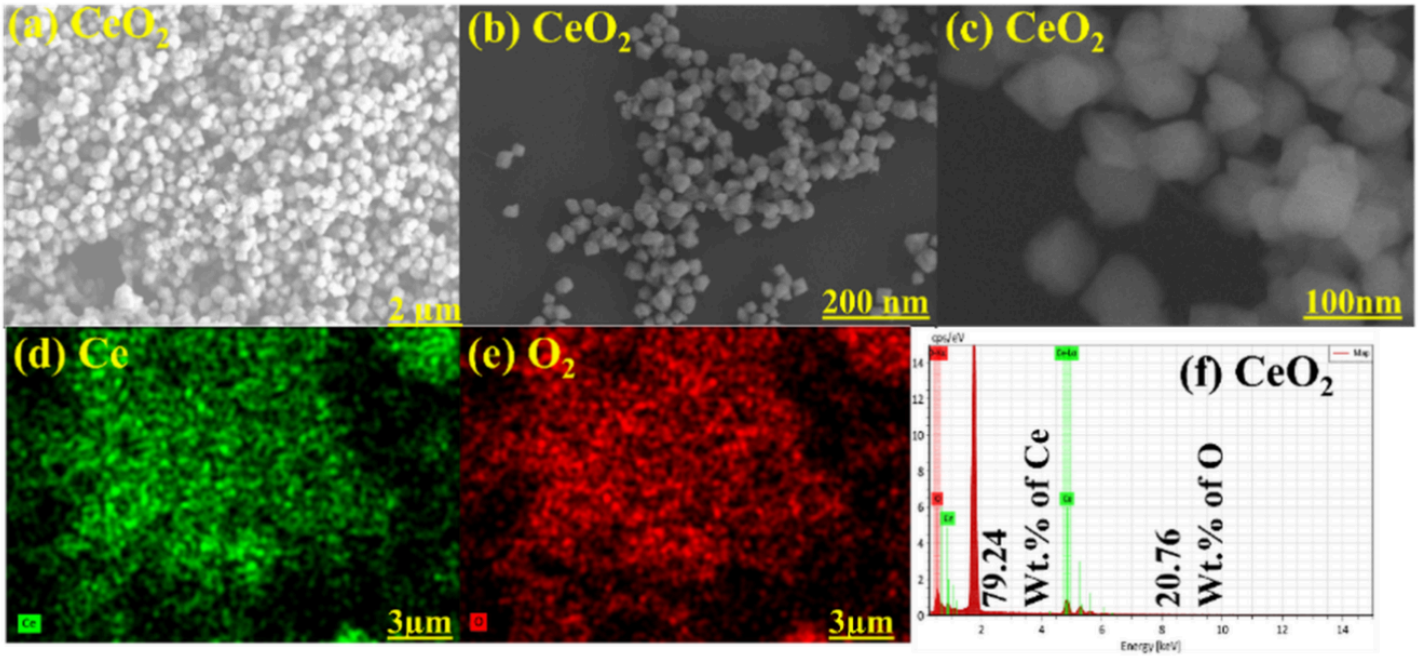


Figure 1

SEM images, Ce and O elemental maps, and EDS spectrum of the octahedral CeO_2 support. The O map corresponds to elemental oxygen

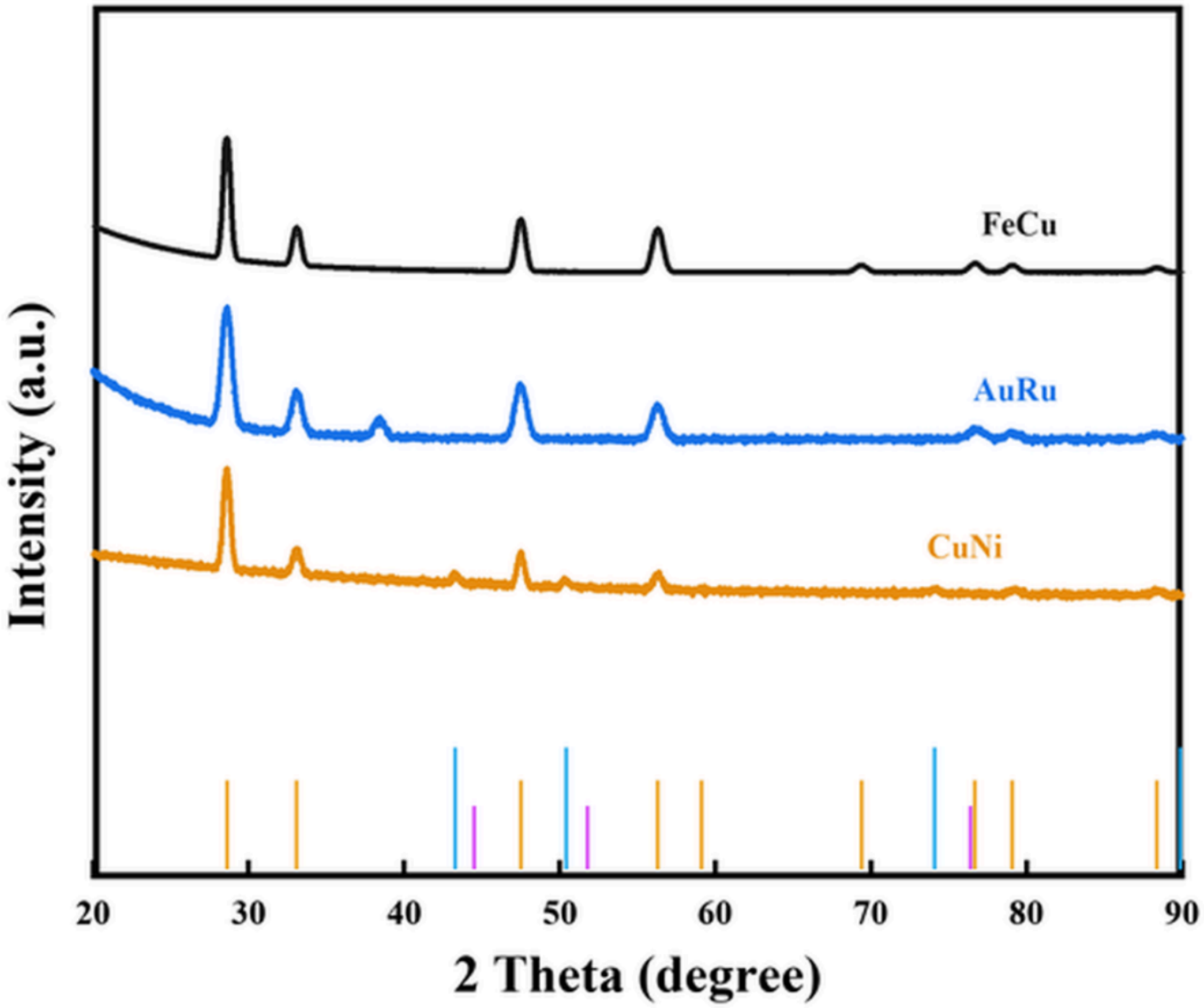


Figure 2

Supplied diffraction illustration with catalyst and reference labels retained; original numerical scans and sample identities remain unresolved, so this illustration is not used to establish detailed phase assignments

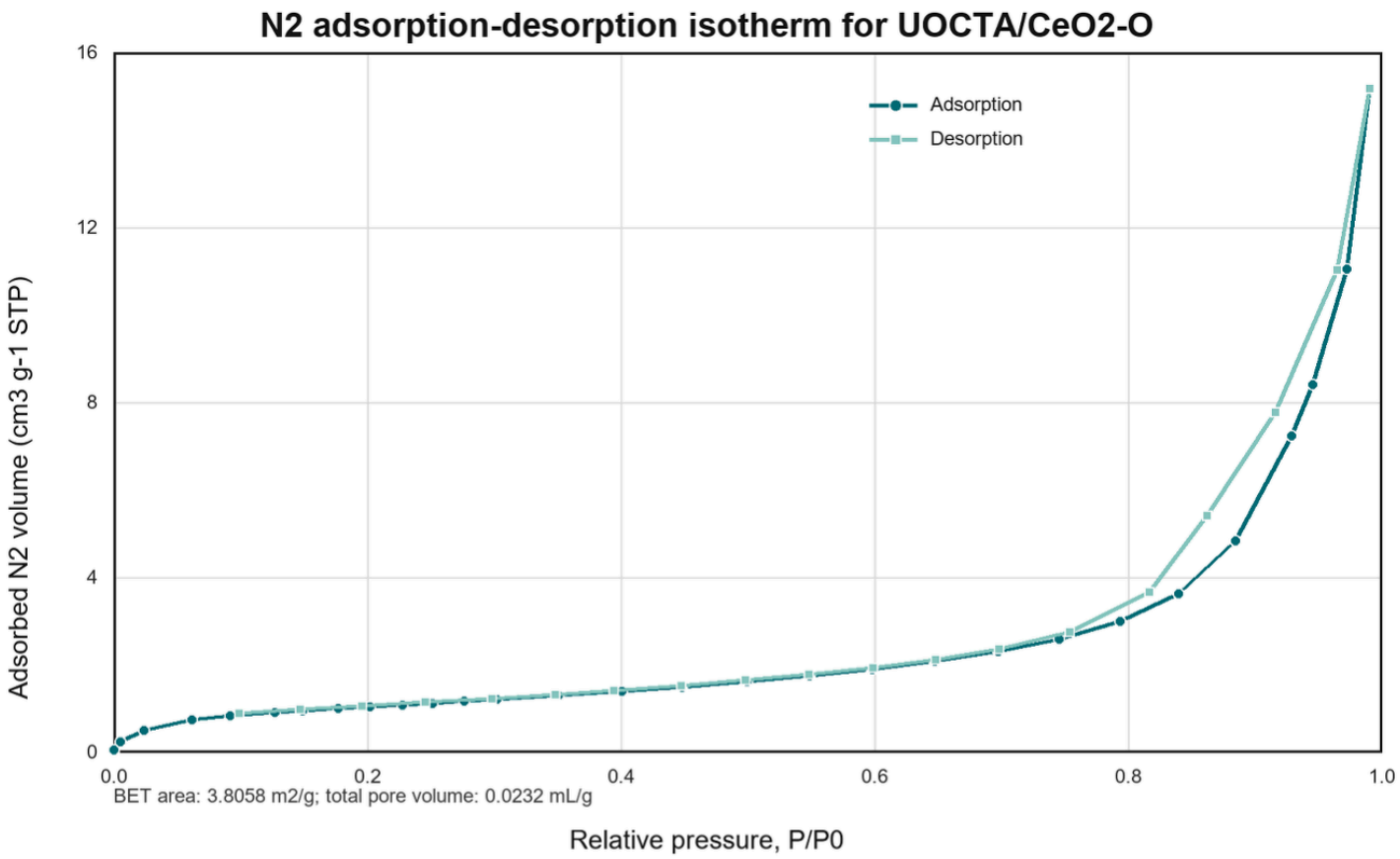


Figure 3

N_2 adsorption-desorption isotherm for octahedral CeO_2-O

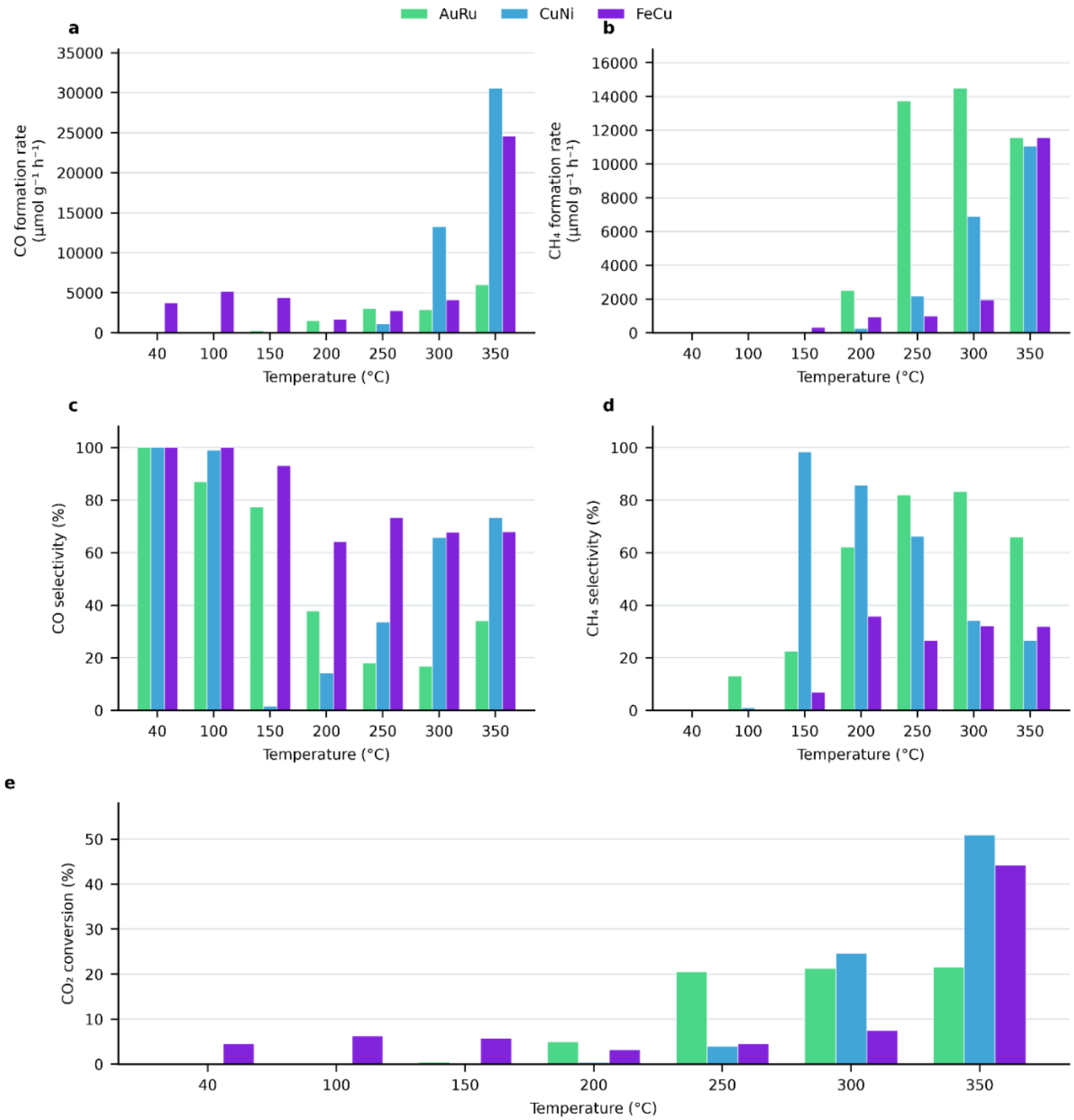


Figure 4

Provisional temperature-dependent summary: (a) CO and (b) CH_4 two-product rate estimates; (c) CO and (d) CH_4 normalized fractions; (e) CO_2 conversion. Sample identity, scaling, mass/flow bases, and zero entries remain unresolved.

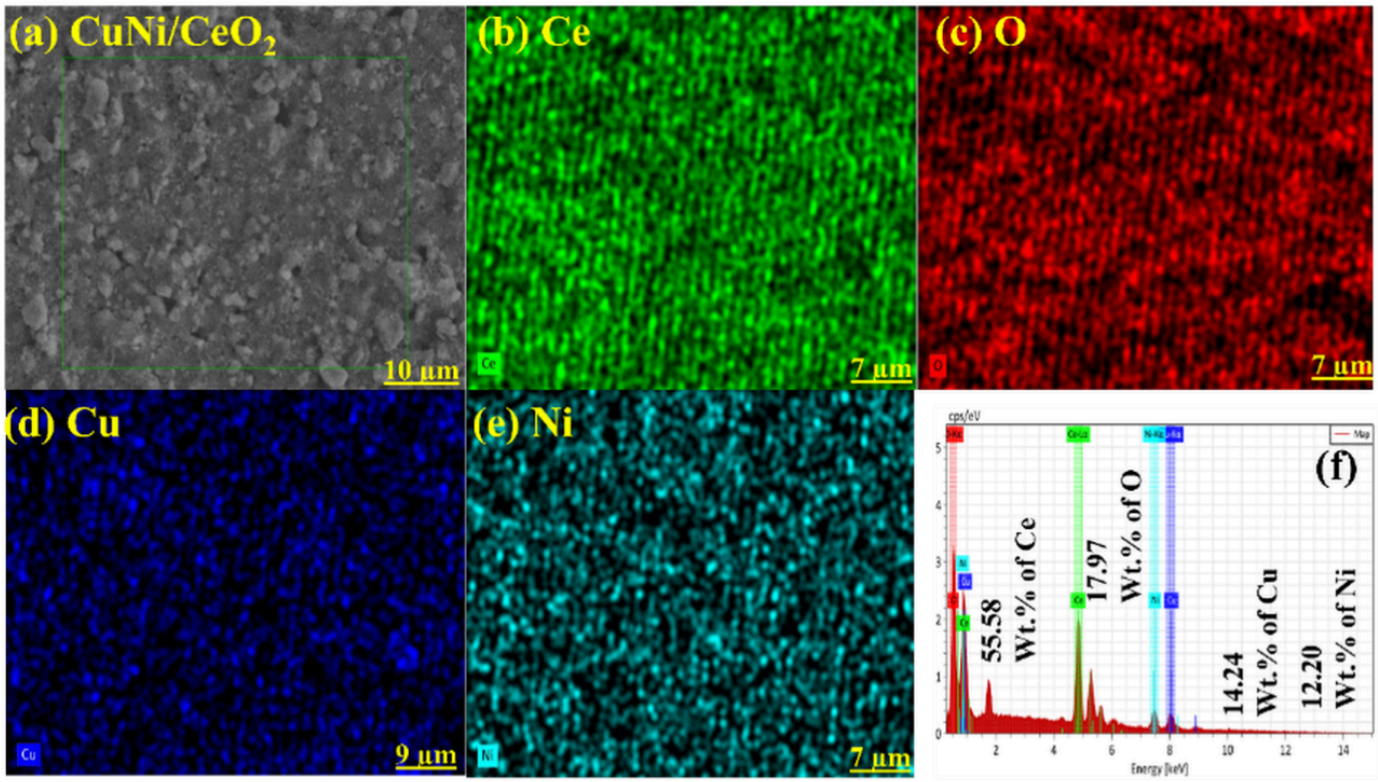


Figure 5

SEM image, Ce/O/Cu/Ni elemental maps, and EDS spectrum of $CuNi/CeO_2$-O

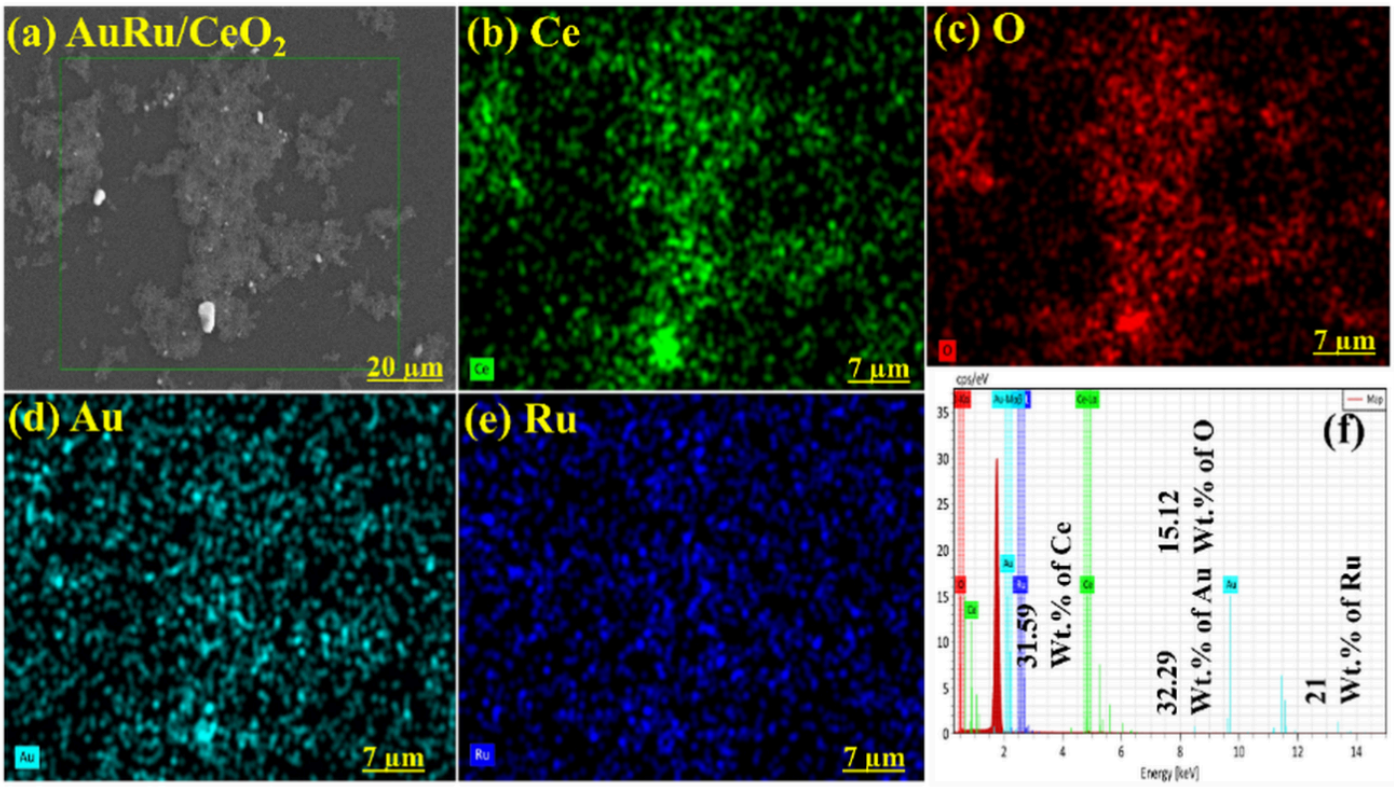


Figure 6

SEM image, Ce/O/Au/Ru elemental maps, and EDS spectrum of AuRu/CeO_2-O

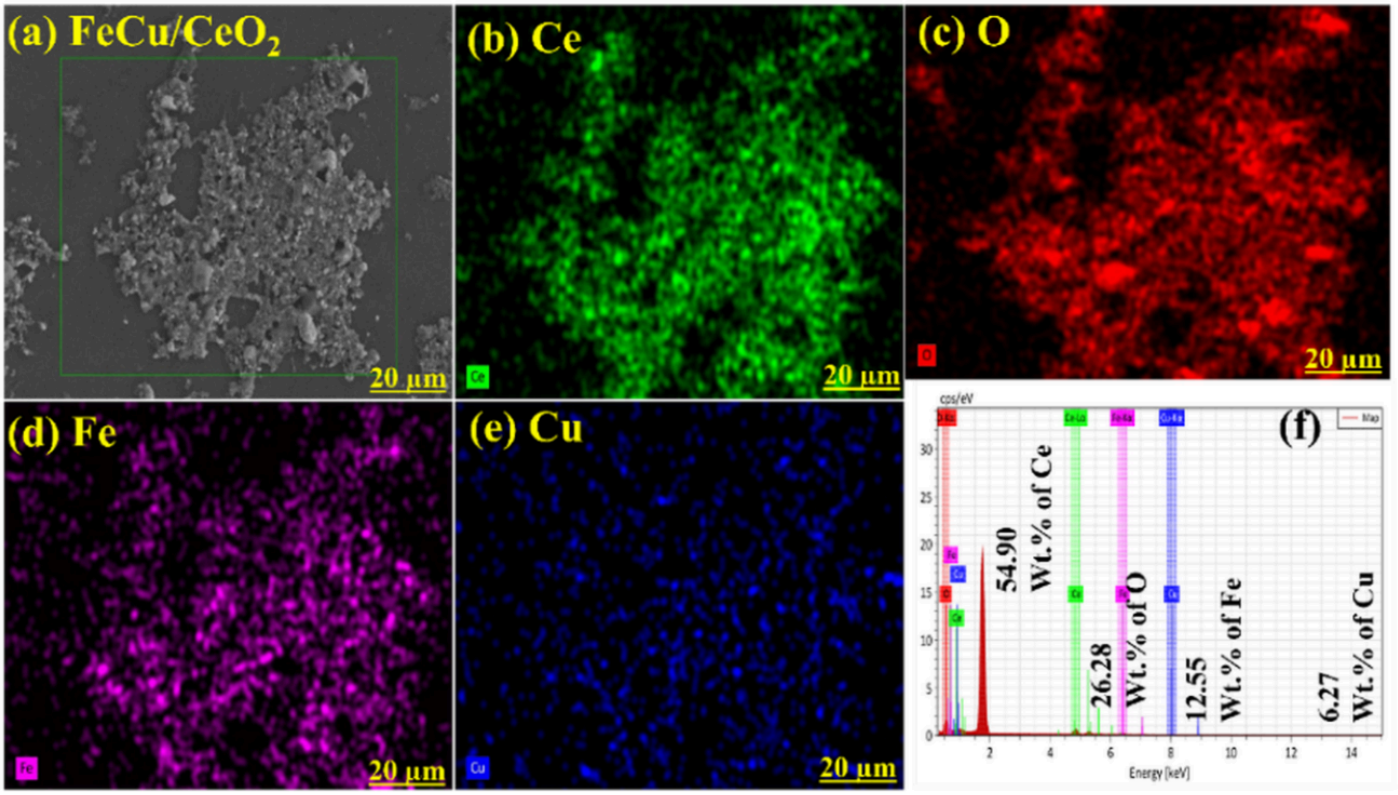


Figure 7

SEM image, Ce/O/Fe/Cu elemental maps, and EDS spectrum of FeCu/CeO_2-O